JGR Atmospheres

RESEARCH ARTICLE
10.1029/2021JD035701

H_2O_2 and CH_3OOH (MHP) in the Remote Atmosphere: 1. Global Distribution and Regional Influences

Hannah M. Allen[1], John D. Crounse[2], Michelle J. Kim[2], Alexander P. Teng[2], Eric A. Ray[3,4], Kathryn McKain[3,4], Colm Sweeney[4], and Paul O. Wennberg[2,5]

[1]Division of Chemistry and Chemical Engineering, California Institute of Technology, Pasadena, CA, USA, [2]Division of Geological and Planetary Sciences, California Institute of Technology, Pasadena, CA, USA, [3]Cooperative Institute for Research in Environmental Sciences (CIRES), University of Colorado Boulder, Boulder, CO, USA, [4]Earth System Research Laboratory, National Oceanic and Atmospheric Administration, Boulder, CO, USA, [5]Division of Engineering and Applied Sciences, California Institute of Technology, Pasadena, CA, USA

This article is a companion to Allen et al. (2022), doi:https://doi.org/10.1029/2021JD035702.

Key Points:

- The Atmospheric Tomography Mission provides an unprecedented investigation into the global seasonal distribution of hydroperoxides
- Chemical Ionization Mass Spectrometry is a sensitive technique for studying hydroperoxides in the remote atmosphere
- Biomass burning emissions increase H_2O_2 mixing ratios in the Atlantic Ocean compared to corresponding latitudes in the Pacific Ocean basin

Supporting Information:

Supporting Information may be found in the online version of this article.

Correspondence to:

H. M. Allen and P. O. Wennberg,
hallen@caltech.edu;
wennberg@caltech.edu

Citation:

Allen, H. M., Crounse, J. D., Kim, M. J., Teng, A. P., Ray, E. A., McKain, K., et al. (2022). H_2O_2 and CH_3OOH (MHP) in the remote atmosphere: 1. Global distribution and regional influences. *Journal of Geophysical Research: Atmospheres*, *127*, e2021JD035701. https://doi.org/10.1029/2021JD035701

Received 13 AUG 2021
Accepted 28 JAN 2022

Abstract Atmospheric hydroperoxides are a significant component of the atmosphere's oxidizing capacity. Two of the most abundant hydroperoxides, hydrogen peroxide (H_2O_2) and methyl hydroperoxide (MHP, CH_3OOH), were measured in the remote atmosphere using chemical ionization mass spectrometry aboard the NASA DC-8 aircraft during the Atmospheric Tomography Mission. These measurements present a seasonal investigation into the global distribution of these two hydroperoxides, with near pole-to-pole coverage across the Pacific and Atlantic Ocean basins and from the marine boundary layer to the upper troposphere and lower stratosphere. H_2O_2 mixing ratios are highest between 2 and 4 km altitude in the equatorial region of the Atlantic Ocean basin, where they reach global maximums of 3.6–6.5 ppbv depending on season. MHP mixing ratios reach global maximums of 4.3–8.6 ppbv and are highest between 1 and 3 km altitude, but peak in different regions depending on season. A major factor contributing to the global H_2O_2 distribution is the influence of biomass burning emissions in the Atlantic Ocean basin, encountered in all four seasons, where the highest H_2O_2 mixing ratios were found to correlate strongly with increased mixing ratios of the biomass burning tracers hydrogen cyanide (HCN) and carbon monoxide (CO). This biomass burning enhanced H_2O_2 by a factor of 1.3–2.2, on average, in the Atlantic compared with the Pacific Ocean basin.

Plain Language Summary Hydroperoxides, a large class of compounds that contain the R–OOH chemical structure, exist in the gas phase in the atmosphere. These compounds are key to the chemistry of the atmosphere because of the role they play in the atmosphere's ability to process and ultimately remove chemical species. Two of the most abundant atmospheric hydroperoxides were measured as part of the Atmospheric Tomography Mission, which collected samples of the atmosphere over the Pacific and Atlantic Ocean basins far from human influences. This paper presents a summary of the global distribution of these hydroperoxides across the four different seasons (winter, spring, summer, fall) and investigates the role that smoke from large-scale fires on the continents plays in altering the amount of atmospheric hydroperoxides above the Atlantic Ocean.

1. Introduction

Atmospheric hydroperoxides are a class of chemical compounds that are of key significance due to their role in altering the oxidizing power of the atmosphere via their connection to the atmosphere's main oxidant HO_x (OH and HO_2 radicals). Hydroperoxides consists of a wide variety of compounds with the linking trait of containing an ROOH functional group, of which hydrogen peroxide (H_2O_2) and methyl hydroperoxide (MHP, CH_3OOH) are generally the most abundant. H_2O_2 in the atmosphere is formed primarily through the self-reaction of HO_2:

$$HO_2 + HO_2 \rightarrow H_2O_2 + O_2 \quad (1)$$

MHP primarily derives from the oxidation of methane (CH_4); CH_4 reacts with OH to form the methyl peroxy radical (CH_3OO) that subsequently reacts with HO_2 to form MHP:

$$CH_4 + OH \rightarrow CH_3OO + H_2O \quad (2)$$

$$CH_3OO + HO_2 \rightarrow CH_3OOH + O_2 \quad (3)$$

The photochemistry of other larger organic molecules, such as acetone, can also lead to methyl peroxy radical (CH_3OO) formation. Both the H_2O_2 and MHP formation reactions depend upon the local NO_x environment: high NO_x (NO and NO_2) limits the formation of H_2O_2 and MHP because NO competes with HO_2 for reaction with the intermediate peroxy radicals; low NO_x environments, such as occur in the remote atmosphere far from major NO_x sources, promote hydroperoxide formation. As a result of this competition, H_2O_2 and MHP are tracers for chemical regimes in which $HO_2 + RO_2$ chemistry is dominant.

Once formed, H_2O_2 and MHP have a lifetime of a day or two in the atmosphere. Physical processes such as deposition remove hydroperoxides in the boundary layer where turbulent winds are present (Chang et al., 2004; Nguyen et al., 2015; Walcek, 1987) whereas convection can move hydroperoxides to remote regions of the atmosphere, including the upper troposphere and lower stratosphere (Jaeglé et al., 1997, 2000). Hydroperoxides also undergo chemical loss through photolysis or reaction with OH, both of which release HO_x back into the atmosphere (Lee et al., 2000). The relative importance of the different hydroperoxide loss mechanisms has a considerable impact on the distribution of H_2O_2 and MHP and results in highly variable hydroperoxide concentrations around the globe. Because H_2O_2 and MHP serve as both a reactive sink and a mobile reservoir of HO_x, understanding their distribution and the factors that contribute to this variability provides insight into the contribution of hydroperoxides to the global HO_x budget (Reeves & Penkett, 2003).

Several studies have investigated hydroperoxide distributions in the remote atmosphere, but due to the nature of sampling have typically been limited. Shipboard deployments have measured hydroperoxides in the remote marine boundary layer across several degrees of latitude (Fischer et al., 2015; Jacob & Klockow, 1992; Kim et al., 2007; Martin et al., 1997; Slemr & Tremmel, 1994; Weller & Schrens, 1993). Airborne measurements have typically sampled only one target area. Prior to this study, the most comprehensive aircraft campaign was the NASA Global Tropospheric Experiment (GTE) program in which hydroperoxides were measured during deployments sampling different paths in the western Pacific (September–October 1991 and January–February 1993), in the tropical Pacific (September–October 1996), and in the tropical Atlantic (September–October 1992; Lee et al., 1998; O'Sullivan et al., 1999). However, this campaign made only limited measurements in the polar and extra-polar regions or in the northern Atlantic, and was limited temporally. Other campaigns have filled in some of these gaps, such as aircraft flights in the Arctic and North Atlantic in fall 1997, winter-spring 2000, summer 2004, and spring-summer 2008 (Mao et al., 2010; Olson et al., 2012; Snow et al., 2003, 2007) or ground measurements made in Antarctica in the austral summers of 2000–2002 (Frey et al., 2005). However, with the exception of a satellite-based investigation of H_2O_2 above 5 km altitude (Allen et al., 2013), no studies have provided a comprehensive set of hydroperoxide measurements that capture remote atmospheric hydroperoxide distributions across latitude, longitude, altitude, and time of year.

Global measurements of H_2O_2 and MHP concentrations in the remote atmosphere with near pole-to-pole coverage were collected as part of the Atmospheric Tomography (ATom) Mission aircraft campaign that took place between summer 2016 and spring 2018. The goal of the campaign was to acquire a comprehensive suite of global-scale tomography data for reactive gases and aerosols in order to understand the chemical and physical processes controlling atmospheric composition (Prather et al., 2017). These measurements were collected without consideration of cloud conditions, except when necessitated for aircraft safety or by air traffic control, thus reducing the clear-sky bias of many prior aircraft campaigns. The campaign sought to investigate the remote atmosphere over the Pacific and Atlantic Ocean basins, far from major land masses and anthropogenic influences. The remote atmosphere is where a significant portion of global atmospheric chemistry occurs, and comprises some of the cleanest, most sensitive areas of the atmosphere; it is therefore the region most susceptible to changing anthropogenic influences. However, the remote atmosphere is poorly sampled and therefore not well constrained in atmospheric models, hampering insight into how well current models capture the changing chemistry of the globe (Brune et al., 2020; Prather et al., 2018; Travis et al., 2020).

In this study, global climatological assessments of H_2O_2 and MHP across the four seasons based on observations from the ATom Mission, are presented for the first time. We discuss the chemical ionization mass spectrometry technique used to measure the hydroperoxide mixing ratios and how these techniques were implemented on the DC-8 during the ATom Mission. We then present the results of these measurements, including regional variations in H_2O_2 and MHP across the northern, mid, and southern Pacific and Atlantic Ocean basins. Finally, we highlight the significant impact of biomass burning in enhancing regional H_2O_2 production. Biomass burning has been posited as a source of atmospheric hydroperoxides, either through primary or secondary chemical production

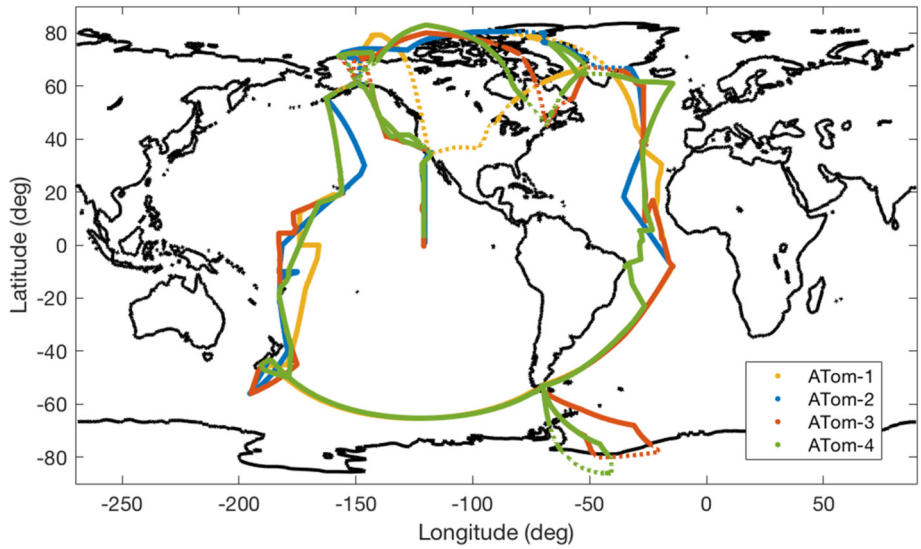

Figure 1. Map of the ATom campaign flight track. The four deployments encompass each of the four seasons (boreal listed): ATom-1 in August 2016 (summer), ATom-2 in February 2017 (winter), ATom-3 in October 2017 (fall), and ATom-4 in May 2018 (spring). Each deployment consisted of 11–13 flights with nearly continuous vertical profiling between 150 m and 13.5 km above ground level along the flight track. Excluded over land data shown as dashed lines.

(Lee et al., 1997; Rinsland et al., 2007; Snow et al., 2007). A companion paper will further describe the chemical and physical controls on global hydroperoxide mixing ratios through comparisons between measurements and chemical models.

2. Methods

2.1. Atmospheric Tomography Mission

During the ATom Mission, over 20 unique instruments were installed aboard the NASA DC-8, which is a Douglas DC-8 jetliner aircraft that has been retrofitted to house the flying laboratory. These instruments collected a variety of physical and chemical data, including meteorological parameters, actinic fluxes, reactive nitrogen species (NO_y), volatile organic compounds (VOCs), photochemical products and oxygenates, aerosols, greenhouse gases, O_3 depleting substances, and a variety of chemical tracers. For the majority of instruments, inlets located along the aircraft walls and windows brought ambient air into the aircraft cabin where the instrument detectors and controls were located. The extensive payload aboard the DC-8 enabled a wide range of chemical and physical phenomena to be investigated.

During ATom the DC-8 flew sequential vertical profiles over the remote Pacific and Atlantic Ocean basins in four separate month-long deployments. The deployments were scheduled to capture variation across each of the four seasons (boreal listed): ATom-1 in August 2016 (summer, 7/29/16–8/23/16), ATom-2 in February 2017 (winter, 1/26/17–2/21/18), ATom-3 in October 2017 (fall, 9/28/17–10/27/17), and ATom-4 in May 2018 (spring, 4/24/18–5/21/18). Each deployment consisted of 11–13 flights that followed a prescribed flight track to gather atmospheric cross-sectional data above the Pacific, Southern, Atlantic, and Arctic Oceans from latitudes spanning −85° to 85° (Figure 1). Two deployments, ATom-3 and -4, additionally included a flight to sample the atmosphere beneath the stratospheric O_3 hole above Antarctica. Along the flight track, the DC-8 underwent sequential slow ascents and descents to generate vertical profiles of the atmosphere, with profiles ranging from about 150 m to just under 13.5 km and therefore sampling from the marine boundary layer (MBL) to the upper troposphere and lower stratosphere (UTLS). Each profile (decent and ascent) took approximately 1 hr of flight time. In total, approximately 320 profiles were collected over the four global circuits. These profiles were conducted to capture the large-scale variability that exists and to ensure unbiased sampling of the atmosphere. In addition, ATom was primarily flown over the remote ocean, but did pass over land masses due to requirements of the flight plan or travel logistics; all data present here have been filtered such that the data exclude measurements collected over land.

2.2. CIT-CIMS

Gas-phase hydroperoxides were measured using the California Institute of Technology Chemical Ionization Mass Spectrometers (CIT-CIMS), a dual instrument that combines a compact Time-of-Flight mass spectrometer (C-ToF, Tofwerk/Caltech) with a triple quadrupole mass spectrometer (Varian/Caltech). Both instruments employ a soft chemical ionization technique to detect oxygenated compounds with high sensitivity. The technique utilizes a CF_3O^- ion as a reagent that reacts with a variety of analytes to form anion products via two primary pathways: by transfer of a fluorine atom (Equation 4) or by clustering with the analyte (Equation 5).

$$X + CF_3O^- \rightarrow X^-_{-H} \cdot HF + CF_2O \quad (4)$$

$$X + CF_3O^- \leftrightarrow X \cdot CF_3O^- \quad (5)$$

The dominant pathway depends upon the acidity (or fluoride affinity) of the analyte, with less acidic compounds, such as hydroperoxides, more likely to undergo clustering with the reagent ion (Paulot et al., 2009). Analytes that undergo fluoride transfer are detected at an m/z of analyte mass +19 (Equation 4) while analytes that undergo reagent ion clustering are detected at an m/z of analyte mass +85 (Equation 5). The CIMS technique and instrument details are further described in Crounse et al. (2006) and St. Clair et al. (2010) and summarized below, including updates to the instruments since previous publication.

The CIT-CIMS configuration onboard the NASA DC-8 consisted of the dual instrument bolted to the floor or wall of the interior of the aircraft with a shared inlet that extended to the outside of the aircraft. Ambient air flowed through a tapered aluminum inlet at a high flow rate traveling in the same direction as the aircraft; a fraction of the air was directed perpendicularly toward the instrument through a rear-cut inlet port. This inlet configuration enabled discrimination against large particles and other debris that had the potential to clog the inlet port. Upon redirection, the ambient air sample was brought to the interior of the aircraft through a Pyrex glass tube, which was coated with a thin layer of fluoropolymer (Fluoropel PFC 801A, Cytonix Corp.) to reduce surface hydrophilicity and reduce loss to inlet surfaces. The air passed through the glass tube at a high rate (~40 m s^{-1}) and short residence time (<0.02 s) thereby further reducing losses to wall effects (see, e.g., Crounse et al., 2006). The glass tubing ended at the "Y-block," a junction that directed air into three separate streams: the C-ToF instrument, the triple quadrupole instrument, and the remainder exited the aircraft via an exhaust outlet (Figure S1 in Supporting Information S1).

For the C-ToF, the ambient air passed through a variable pinhole orifice and into a second Pyrex glass flow tube coated with hydrophobic fluoropolymer. The pinhole orifice automatically adjusted to control the flow tube pressure to a static set point (35 mbar) and resulted in a nominally constant mass flow of ambient air into the instrument (300–350 standard cubic centimeters per minute or sccm) with relatively small variations caused by changing flow tube temperature. Upon entering the flow tube, the sample was diluted with with dry N_2 (1,300 sccm) before interacting with the reagent ion. This dilution reduced the water mixing ratio as high water content interferes with analyte-ion clustering and increases background signals. The reagent ion was formed by passing 380 sccm of 1 ppm CF_3OOCF_3 in N_2 through a cylindrical ion source containing a layer of radioactive polonium-210 (Po-210, NRD LLC, ≤10 mCi). Ions are sampled into the mass filter through a pinhole orifice and then focused by a conical hexapole ion guide into the C-ToF mass spectrometer chamber. Compounds are separated in the mass spectrometer based on differences in their mass-to-charge ratio as an electric field accelerates them through the instrument. During ATom, the C-ToF data was used to report ambient mixing ratios at a 1 Hz frequency for H_2O_2 (m/z = 119), hydrogen cyanide (HCN, m/z = 112), nitric acid (HNO_3, m/z = 82), peroxyacetic acid (PAA, m/z = 161), peroxynitric acid (PNA, m/z = 98), and sulfur dioxide (SO_2, m/z = 83 and 101). The C-ToF was also used to report MHP (m/z = 133) mixing ratios at 1 Hz frequency for ATom-4, with the triple quadrupole used for the other three deployments.

The ambient sample directed to the triple quadrupole mass spectrometer was diluted and ionized in a similar manner to that of the C-ToF. From the "Y-block," an approximately 1.5 m length of Teflon tubing carried the sample at a high flow to the "T-block," where a small flow (~350 sccm) passed through a pressure controlled pinhole orifice into the fluoropolymer-coated Pyrex flow tube (35 mbar). The sample was diluted with dry N_2 (1,450 sccm) and mixed with a calibration gas (isotopically labeled MHP, CD_3OOH) then ionized with CF_3O^- before passing through a second pinhole orifice and a series of lenses into the mass spectrometer chamber. The mass spectrometer is a modified Varian 1200 GCMS that contains three quadrupoles. Upon entering the mass

spectrometer, the first quadrupole performs a mass filtration of the analyte stream; the selected primary ions pass to the collision-induced dissociation (CID) quadrupole region in which collision N_2 molecules causes fragmentation of the analyte ions; finally, a third quadrupole filters for specific secondary ions produced by the CID. This methodology enables the mass spectrometer to differentiate certain nominally isobaric compounds, which are indistinguishable on the C-ToF, by decomposing the parent ion into a unique pattern of secondary ions. As a result, analytes are detected by both the primary and secondary m/z signals. The triple quadrupole monitored MHP at $m/z = 133 \rightarrow m/z = 85$ and isotopically labeled MHP calibration gas at $m/z = 136 \rightarrow m/z = 85$. MHP mixing ratios are reported for the first three ATom deployments as 1 s averages every 10–15 s.

The flight pattern pursued during ATom resulted in a wide range of temperatures, pressures, and water vapor concentrations during sampling. Because the instrument measurements are sensitive to the temperature and water vapor mixing ratios in the ion-molecule reaction region (Figure S2 in Supporting Information S1), the CIT-CIMS was calibrated extensively in the laboratory, as well as during each ATom science flight. In the laboratory, the instruments were calibrated by introducing a known quantity of the desired compound—verified by FTIR, gravimetric analysis, or other analytical method—into the instruments and monitoring the signal as a function of water vapor. Pre-flight and in-flight calibrations were performed by introducing a small flow into the instrument from temperature-controlled diffusion vials containing either PAA or isotopically labeled MHP or a U-tube containing urea-H_2O_2. The reported MHP mixing ratios from the triple quadrupole instrument relied upon a continuous injection of labeled MHP (CD_3OOH) during the flights and used the ratio of ambient MHP to the labeled MHP to account for water vapor and temperature-dependent variations in the instrument sensitivity, a method that was introduced just prior to the ATom deployments.

Uncertainty in the CIT-CIMS measurements during ATom arose from a combination of uncertainty in instrument precision, background corrections, and in each of the applied calibrations: water-dependency, temperature-dependency, and absolute sensitivity. The uncertainty in instrument precision and in the absolute sensitivity, arising primarily from uncertainty in FTIR fits, persists across all measurement regimes and deployments. For the ToF H_2O_2 and MHP measurements, this uncertainty is 50 pptv (parts per trillion by volume) + 30% of the measurement value; for the triple quadrupole MHP, this uncertainty is 25 pptv + 30% of the measurement value. The minimum detection limit of the C-ToF and the triple quadrupole depends upon several factors, and is typically in the low (1–10) pptv range for hydroperoxides under dry conditions. However, the ToF instrument sensitivity toward hydroperoxides declines rapidly at high water vapor and high temperature (Figure S2 in Supporting Information S1); therefore MHP mixing ratios for ATom-4 are not reported above water mixing ratios of 7,500 ppmv. In addition, the mass at which MHP is measured has a potential interference due to atmospheric methylene diol ($HOCH_2OH$, $m/z = 133$). Because this compound arises from formaldehyde and water, it is expected to be most prevalent in regions with high water vapor (e.g., the marine boundary layer), which corresponds to regions in which instrument sensitivity toward MHP is low (Figure S3 in Supporting Information S1). Further details about the calibrations and an estimate of the extent of the methylene diol interference are given in the Supporting Information.

In addition to calibrations, two forms of zeroing occurred periodically during science flights to assess instrument background signals and interferences. A dry zero was performed by closing the inlet orifice, thereby preventing the ambient sample from entering the flow tube, and increasing the flow of dry N_2 to maintain 35 mbar in the flow tube. An ambient zero was performed by passing ambient air through a bicarbonate denuder and bicarbonate-coated nylon wool and palladium filter to remove compounds of interest but retain water vapor, thus monitoring background signals at the same relative humidity as was present in ambient samples. The data from each instrument were normalized to the sum of the ^{13}C reagent ion signal ($^{13}CF_3O^-$, $m/z = 86$) and reagent ion water cluster ($^{13}CF_3O^- \cdot H_2O$, $m/z = 104$) to correct for changes in the reagent ion current and then corrected for background interferences. A new synthetic approach to producing CF_3OOCF_3 was developed between ATom-2 and ATom-3, which greatly reduced known impurities in the synthetic mixture as the new CF_3OOCF_3 material reduced instrumental background signals for SO_2 and SF_6 by more than a factor of 50 (see the Supporting Information for further details). In addition, careful avoidance of using new PFA tubing in the plumbing reduced the background signals of m/z 133 in the ToF (likely arising from out-gassing of $CF_3C(O)OH$ from PFA) such that MHP could be measured from this instrument for ATom-4.

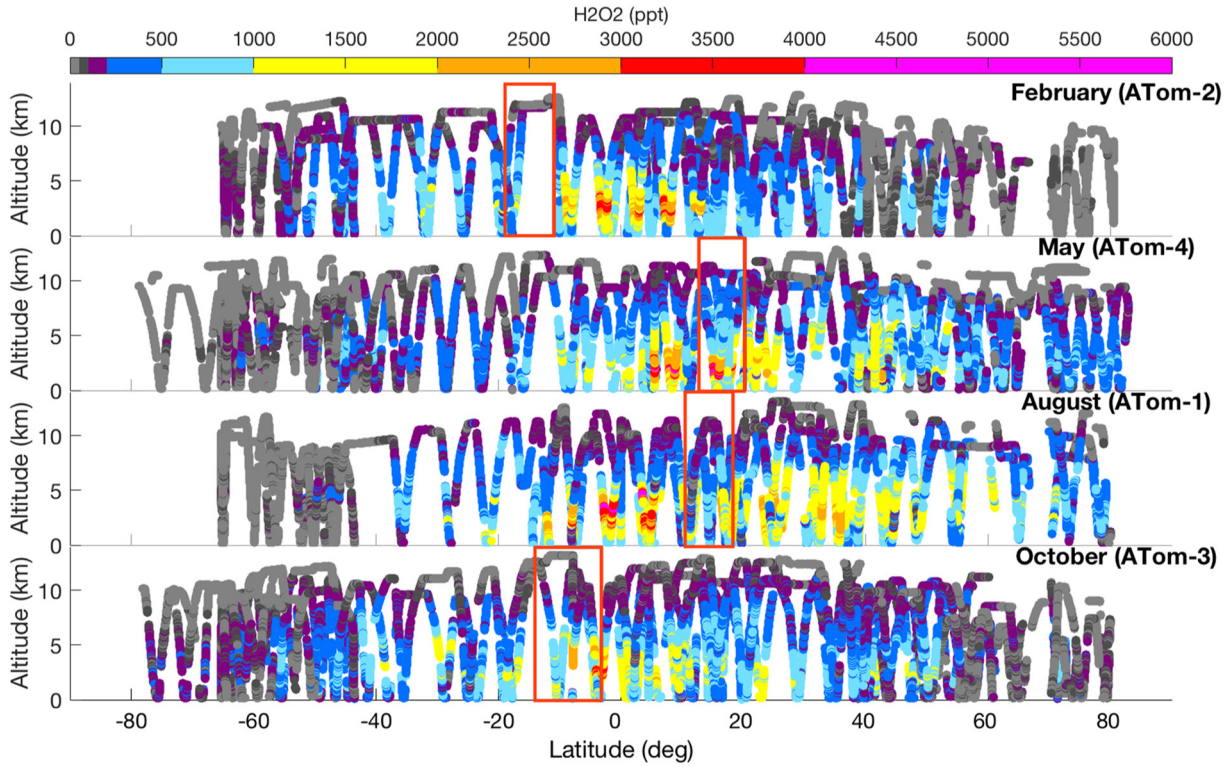

Figure 2. Mixing ratios of H_2O_2 across latitude and altitude. H_2O_2 mixing ratios dominate in the equatorial latitudes, but extend poleward with some progression due to time of year. Red boxes indicate the range of subsolar point latitudes during the deployment. Note at the low end of the color scaling is light gray (<50 pptv), dark gray (50–100 pptv), purple (100–200 pptv), and dark blue (200–500 pptv). Excludes data collected over land.

3. Results and Discussion

3.1. Global Cross Sections

The global hydroperoxide distribution shows characteristic latitude and altitude patterns, as can be seen in Figures 2 and 3. These figures show latitude-altitude cross-sections of global H_2O_2 and MHP, respectively, collected during each of the four ATom deployments; they do not make a distinction between the Pacific and Atlantic Ocean basins. Because hydroperoxide formation and major loss mechanisms are highly dependent on photochemistry, the subsolar point, the latitude at which the sun's rays are perpendicular to Earth's surface at noon, indicate where this photochemistry is most prominent. During the ATom deployments, the subsolar point varied from approximately −19° to −11° latitude in February, 13° to 20° in May, 10° to 18° in August, and −14° to −3° in October. In addition, the marine boundary layer height, which also affects hydroperoxide formation and loss, varied between approximately 50 and 2,500 m above sea level during the deployments.

For all four deployments, mixing ratios for both hydroperoxides peak in the equatorial region (−20° to 20° degrees latitude); however, the range of latitudes over which the hydroperoxide mixing ratios extend varies by season. Except for the northern hemisphere in August, H_2O_2 mixing ratios rarely reach high mixing ratios (>1,000 pptv) in the polar regions (latitudes >60° or <−60°). In February, high H_2O_2 mixing ratios extend from latitudes of −45° to 20°, whereas in August high H_2O_2 mixing ratios reach a much wider and more northern latitudinal range of −30° to near 70° (Figure 2). This shift follows the progression of sunlight and temperature as global photochemistry shifts northward in the boreal summer. Similarly, MHP mixing ratios show a seasonal shift hemispheric distributions, although the pattern is not as pronounced as is that of H_2O_2. In February, for example, high MHP mixing ratios (>1,000 pptv) reach 30–40° wider latitude range than those of H_2O_2 (Figure 3). This trend likely reflects the difference in hydroperoxide lifetimes due to deposition. MHP has a longer atmospheric lifetime than H_2O_2 because it is far less soluble ($\sim 10^3$ difference in Henry's Law constants; Lee et al., 2000), leading to more efficient poleward transport.

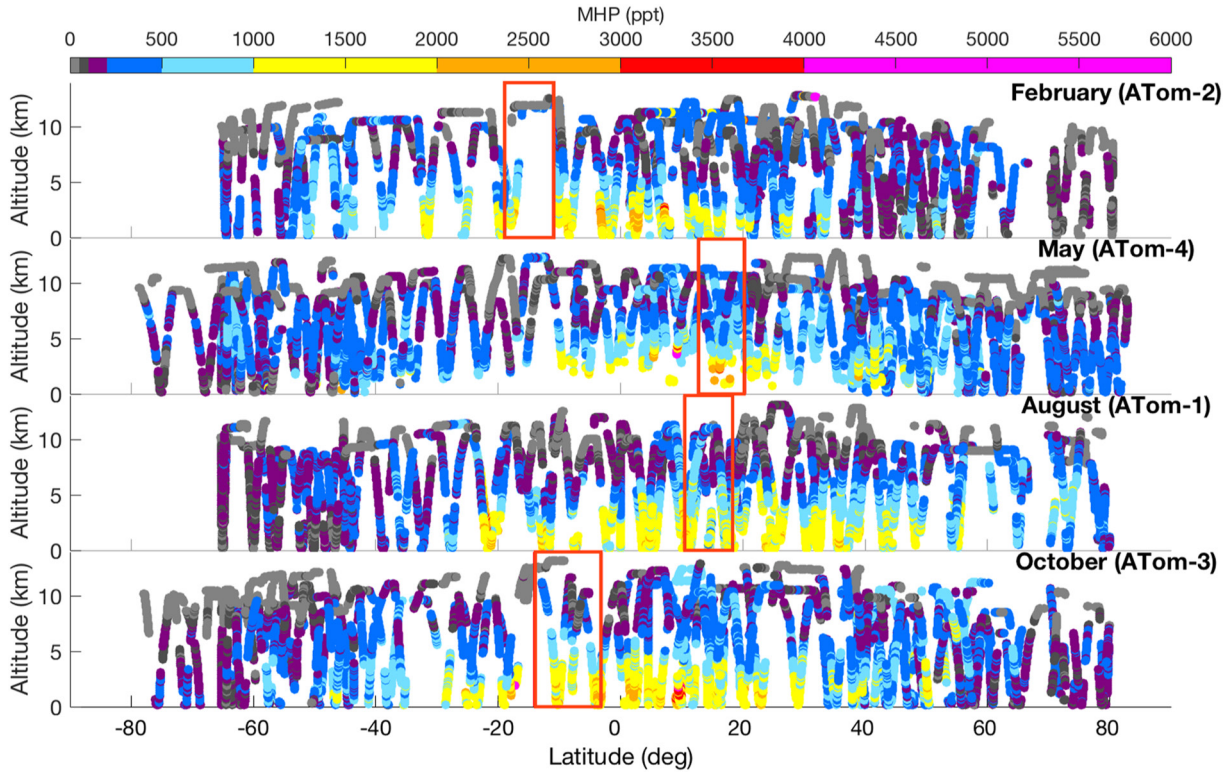

Figure 3. Mixing ratios of MHP across latitude and altitude. MHP mixing ratios show a wide distribution across latitudes as well as a shift between northern and southern hemispheric maximums due to time of year, though the pattern is not as pronounced as for H_2O_2. Red boxes indicate the range of subsolar point latitudes during the deployment. See Figure 2 for a note on color scaling. Excludes data collected over land.

The column variations in H_2O_2 and MHP mixing ratios show distinct patterns in season and poleward direction. Column averages for H_2O_2 and MHP were found by removing stratospheric measurements (regions with $O_3 > 100$ ppbv above 7 km altitude) and averaging all tropospheric altitudes in 1° latitude bands. For H_2O_2, the decrease with latitude is typically faster in the southern hemisphere than the northern hemisphere. For the northern hemisphere, the column average declines by 4.5, 4.2, 2.7, and 4.8 pptv per degree latitude for February, May, August, and October, respectively; whereas in the southern hemisphere the column average decreases by 6.7, 4.1, 9.7, and 5.4 pptv per degree latitude for February, May, August, and October, respectively. By comparison Van Valin et al. (1987) measured a much faster decline of 40–50 pptv per degree of latitude increase, but measured over the continental United States rather than over the ocean in the remote atmosphere. The decline in column average MHP mixing ratios is very similar to that of H_2O_2, although note that the high water interference in the MHP measurements for ATom-4 (May) alters the averages for this deployment. In the northern hemisphere, the rate of column average MHP decrease is 4.6, 2.9, 3.9, 5.5 pptv/degree latitude, while in the southern hemisphere the decline is 6.1, 0.7, 6.4, and 7.5 pptv/degree latitude for February, May, August, and October, respectively.

3.2. Regional Profiles

The profiles of H_2O_2 and MHP mixing ratios averaged with altitude indicate clear structure that persists regardless of season. Figure 4 shows the ATom data averaged over 0.5 km altitude bins for the northern (20° to 60°), mid (−20° to 20°), and southern (−60° to −20°) latitude bands of the Pacific and Atlantic Ocean basins. In nearly all regions, the average H_2O_2 and MHP mixing ratios peak just above the boundary layer and decline with altitude in the free troposphere. For H_2O_2, this peak occurs between 2 and 4 km above the ocean surface while the peak MHP mixing ratio is typically at a slightly lower altitude (1–3 km). Both hydroperoxides exhibit a gradient in the marine boundary layers with lower mixing ratios close to the ocean surface, although this feature is more pronounced for H_2O_2. In the mid-Atlantic where the gradient is the strongest, maximum MHP mixing ratios are a factor of 1.3–1.7 times higher than within the boundary layer, compared with a factor of 2.5–4.1 times for H_2O_2.

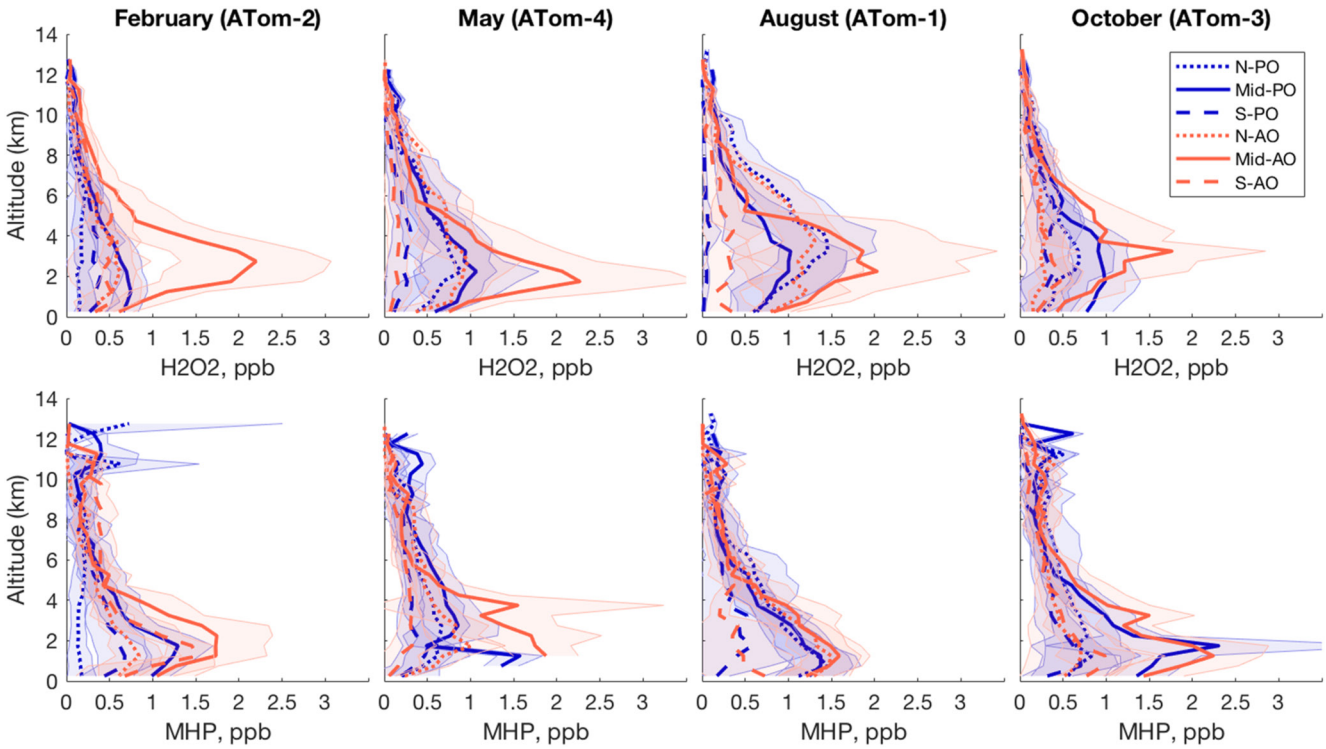

Figure 4. Average H_2O_2 and methyl hydroperoxide mixing ratios with altitude for different ocean basin regions. The hydroperoxides are averaged over 0.5 km altitude bins and separated into north (20° to 60°) mid (−20° to 20°), and south (−60° to −20°) latitude bands of the Pacific (blue) and Atlantic (red) ocean basins. The shaded region indicates the standard deviation of the mean.

H_2O_2 has a higher Henry's Law coefficient than MHP (1×10^5 M atm^{-1} and 5×10^2 M atm^{-1} at 298 K, respectively; Lee et al., 2000) and therefore is more subject to deposition and wet scavenging that occurs in the turbulence of the mixed layer than MHP. Finally, the MHP profiles reveal a secondary peak in mixing ratios at altitudes above 8,000 m, not observed in the H_2O_2 profiles. Because MHP is less soluble than H_2O_2, it can be transported to the upper troposphere and lower stratosphere via convection (Barth et al., 2016; Jaeglé et al., 1997).

For the majority of the deployments, the average H_2O_2 mixing ratio was larger over the Atlantic Ocean than the Pacific Ocean (Figure 4 and Figure S4 in Supporting Information S1). This trend is strongest in February, when the maximum H_2O_2 mixing ratio is three times higher in the mid-Atlantic than the mid-Pacific and the mean value is 2 times higher (Table 1). The trend weakens as the year progresses, but the mid-Atlantic to mid-Pacific ratio persists in other seasons (1.6–2.1 for the maximum and 1.1–1.3 for the mean H_2O_2). The mean H_2O_2 mixing ratios are similar to or slightly lower than those measured by other studies, which suggest H_2O_2 reaches mean mixing ratios of 1–3 ppbv (parts per billion by volume) in the remote marine lower troposphere in equatorial regions during the months of September–October (Allen et al., 2013; Lee et al., 1998; O'Sullivan et al., 1999). In contrast to the mid-ocean regions, the northern and southern portion of the Atlantic and Pacific indicate a stronger seasonal role affecting H_2O_2. The northern and southern ocean basins vary by a factor of 2–3 between seasonal maximums or minimums in February and August (Table 1); however, this seasonality is not present in the southern Atlantic Ocean, suggesting that this region may be influenced by other factors.

The difference between the Atlantic and Pacific Ocean basins is smaller for MHP than for H_2O_2. Like H_2O_2, MHP is typically higher in the Atlantic than the Pacific; however the difference is much smaller than for H_2O_2 (Figure 4 and Figure S5 in Supporting Information S1). For example, in August the mid-Atlantic and mid-Pacific maximum MHP mixing ratios are near parity. Similarly, the average MHP mixing ratio between the mid-Atlantic and mid-Pacific varies by a factor of 0.8–1.3, with mid-Atlantic dominating in May and August (Table 2). In May and October, both the northern and southern portions of the Atlantic and Pacific have very similar altitude profiles with weak altitude gradients and little difference between the two ocean basins (factor of 0.9–1.3 difference). In addition, the southern latitudes in February and the northern latitudes in August show profiles with shapes and

Table 1
Statistics[a] of H_2O_2 Mixing Ratios Measured During ATom

		N-PO	Mid-PO	S-PO	N-AO	Mid-AO	S-AO	Arctic	S. Ocean
February	max	980	1,300	1,220	950	4,030	1,490	200	270
(ATom-2)	median	50	130	110	180	250	120	10	20
	mean	110 (1.3)	270 (1.0)	170 (1.1)	270 (0.9)	540 (1.3)	180 (1.2)	30 (1.4)	50 (1.2)
May	max	2,560	3,720	1,380	2,580	6,450	870	960	300
(ATom-4)	median	190	270	60	380	240	40	140	20
	mean	330 (1.1)	410 (0.9)	130 (1.2)	420 (0.9)	550 (1.4)	90 (1.3)	170 (1.0)	30 (1.4)
August	max	2,970	2,950	510	2,670	6,190	1,730	1,920	140
(ATom-1)	median	320	280	30	290	270	70	220	10
	mean	500 (1.1)	470 (1.0)	30 (1.2)	550 (1.0)	610 (1.3)	170 (1.4)	290 (1.0)	10 (1.2)
October	max	1,760	2,330	2,960	1,050	3,630	1,470	1,080	540
(ATom-3)	median	160	190	120	120	200	70	50	30
	mean	250 (1.1)	380 (1.0)	180 (1.2)	180 (1.1)	400 (1.3)	130 (1.3)	90 (1.6)	60 (1.3)

Note. Maximum[b], median, and mean (standard deviation) H_2O_2 mixing ratios are segmented into north (20°–60°), mid (−20°–20°), and south (−60°–20°) latitude bands of the Pacific (PO) and Atlantic (AO) ocean basins, as well as the Arctic Ocean (latitudes >60°) and Southern Ocean (latitudes <−60°). All values are given in pptv except standard deviation, shown as a factor relative to the mean.

[a]Statistics based on 1 s time-averaged data. [b]Minimum values for each region are below detection limits.

peak average mixing ratios similar to those of the mid-ocean basins, indicating the wider latitudinal distribution of MHP than H_2O_2. Overall, the maximum MHP mixing ratios measured during ATom are similar but slightly higher than those measured previously which typically reached up to 1.25–5 ppbv in the equatorial regions and up to 2 ppbv in the northern Atlantic during the late boreal summer and early fall (O'Sullivan et al., 1999; Slemr & Tremmel, 1994; Snow et al., 2007).

Table 2
Statistics[a] of MHP Mixing Ratios Measured During ATom

		N-PO	Mid-PO	S-PO	N-AO	Mid-AO	S-AO	Arctic	S. Ocean
February	max	7,030	3,320	1,430	1,470	3,950	2,290	460	480
(ATom-2)	median	150	300	180	240	310	340	60	10
	mean	230 (2.0)	420 (1.0)	230 (1.1)	320 (0.9)	530 (1.2)	350 (0.9)	80 (1.1)	90 (1.3)
May	max	2,120	2,010	2,970	2,040	6,690	1,280	900	830
(ATom-4)	median	230	400	190	270	160	150	150	100
	mean	300 (0.9)	410 (0.6)	220 (0.9)	320 (0.9)	320 (1.6)	170 (0.9)	160 (0.9)	160 (1.1)
August	max	2,390	2,490	4,340	2,460	2,530	2,420	1,250	350
(ATom-1)	median	230	330	160	210	200	180	290	70
	mean	460 (1.1)	540 (0.9)	240 (1.6)	480 (1.1)	480 (1.1)	280 (1.3)	280 (0.8)	80 (0.8)
October	max	2,590	8,640	1,910	2,200	4,880	2,360	800	540
(ATom-3)	median	280	340	170	260	390	120	150	30
	mean	380 (0.9)	590 (1.2)	230 (1.1)	370 (1.0)	680 (1.1)	220 (1.2)	180 (0.7)	70 (1.2)

Note. Maximum[b], median, and mean (standard deviation) MHP mixing ratios are segmented into north (20°–60°) mid (−20°–20°), and south (−60° to − 20°) latitude bands of the Pacific (PO) and Atlantic (AO) ocean basins, as well as the Arctic Ocean (latitudes >60°) and Southern Ocean (latitudes <−60°). All values are given in pptv except standard deviation, shown as a factor relative to the mean.

[a]Statistics based on 1 s time-averaged data. [b]Minimum values for each region are below detection limits.

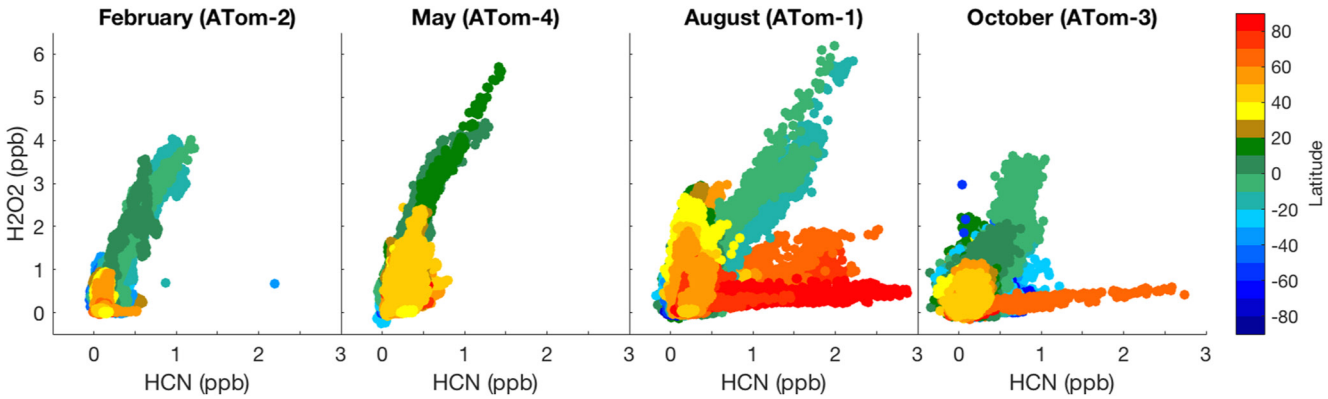

Figure 5. Correlation between H_2O_2 and HCN, colored by latitude. The periods of strong correlation between H_2O_2 and HCN, a major biomass burning tracer, indicates the production of H_2O_2 in regions influenced by biomass burning emissions. These biomass burning plumes occur primarily in the equatorial region (latitudes of −20° to 20°) throughout all times of the year sampled.

3.3. Influence of Biomass Burning

The large asymmetry between the tropical Atlantic and Pacific is correlated with the influence of biomass burning. Particle sampling during the ATom campaign revealed widespread biomass burning smoke throughout the remote troposphere, with both concentrated plumes in the Atlantic basin and extensive impact across the globe observed during all four deployments (Schill et al., 2020). As seen in Figure 5, enhanced H_2O_2 (including the highest measured mixing ratios during the campaign) correlate strongly with HCN. The primary source of HCN in the atmosphere is biomass burning combustion (Li et al., 2000; Singh et al., 2003); therefore the correlation of H_2O_2 with HCN and with another biomass burning tracer carbon monoxide (CO) indicates the significant evolution of H_2O_2 in the chemical aging of biomass burning plumes in the remote troposphere (Figure S6 in Supporting Information S1). These periods of H_2O_2 production occur primarily in the equatorial latitudes between −20° and 20°. Notably, high HCN mixing ratios are also observed during August and October in the Arctic (latitudes >60°), indicating biomass burning plumes in these regions as well. However, these plumes show only minor enhancements in H_2O_2. These northern plumes are likely less photochemically active due to the higher solar zenith angles and higher NO_x levels that compete for hydroperoxide precursor radicals.

In order to better assess the origin and aging of these biomass burning plumes, a 10-day back trajectory analysis was conducted along 1 min intervals of the flight track (see the Supporting Information for further details). The aircraft encountered the regions of high H_2O_2 and HCN at altitudes between 1 and 4 km during either partial or full flights on 08/17/2016 (ATom-1), 02/13/2017 (ATom-2), 02/15/2017 (ATom-2), 10/17/2017 (ATom-3), 10/19/2017 (ATom-3), and 05/14/2018 (ATom-4). These periods were selected by isolating flights in which H_2O_2 reached mixing ratios above 2.5 ppbv and showed a clear correlation with HCN (i.e., HCN reached above 0.5 ppbv in the same period) as per Figure 5; periods were additionally filtered such that the flight path outside 0.5–6.5 km in altitude was excluded. The flights all occurred between the southern tip of South America and the eastern coast of northern Africa, indicating that this influence extended to just the Atlantic Ocean basin. The results of the back trajectory analysis are shown in Figure 6 and indicate that the biomass burning plumes primarily originated from Africa, likely with some secondary influence from S. America, and produced H_2O_2 as the air mass migrated over the Atlantic Ocean during the course of several days as the bulk of the back trajectories passed at high altitudes over a portion of S. America and at low altitudes over a portion of the African continent or its coast.

The region of Africa that the air masses encountered influenced the latitudinal distribution of the H_2O_2 enhancement. In nearly all the deployments, the back trajectories passed over the northern portion of Africa before reaching the aircraft. Africa is the largest source of biomass burning emissions in the world and was responsible for 70% of the total burned area across the globe between 2001 and 2010 (Randerson et al., 2012). However, based on satellite imagery, African biomass burning occurs in the southern portion of the continent (−50° to −20° latitudes) during the boreal summer and fall months and shifts to the northern portion of the continent (−20° to 0° latitudes) during the boreal winter and spring months (Randerson et al., 2012; Roberts et al., 2009). In the February and October deployments, the air masses passed either very close to or directly over the region of heaviest

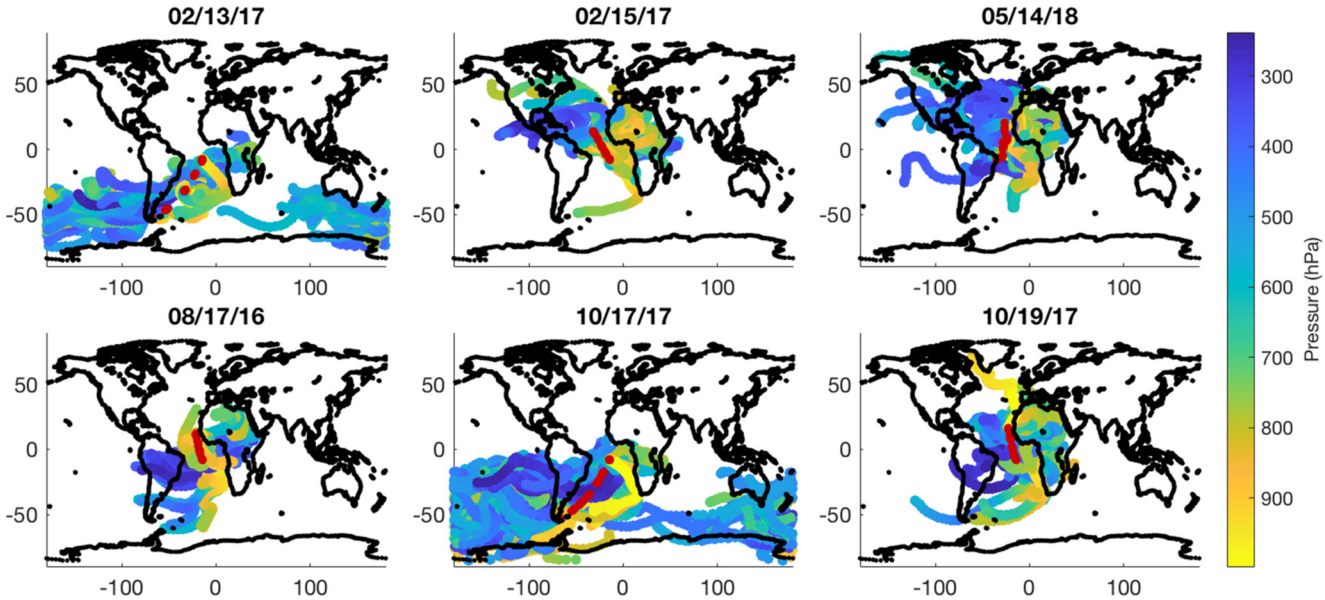

Figure 6. Average longitude, latitude, and pressure (altitude) for 10-day back trajectories of air masses encountered at each 1-min interval along the flight track. Data and flight tracks (red) shown are portions of flights in which a strong photochemically processed biomass burning signature was detected based on a high H_2O_2 and HCN correlation (see Figure 5).

biomass burning (Figure 6). These deployments show the greatest dispersion of biomass burning influence with high H_2O_2 across the full range of the S-AO and mid-AO. The May and August deployments encountered air masses that likely passed near but not directly over the regions of highest biomass burning intensity and although high, the peak H_2O_2 mixing ratios were limited to a section of the mid-AO and less dispersed. In addition, the wind speeds the aircraft encountered during the May and August deployments were low to moderate (speeds of 5–20 m/s) compared with those of the January and October deployments (typically 10–50 m/s), and therefore the air masses likely were more strongly diluted throughout the remote troposphere.

The magnitude of the H_2O_2 enhancement in biomass burning plumes varied by season. Typically, an enhancement ratio ($\Delta X = X_{plume} - X_{bckgnd}$ normalized to that of a long-lived tracer such as CO to account for dilution) would be used to compare in-plume mixing ratios with those of background air (Andreae, 2019). However, due to the nature of sampling during ATom, the enhancement ratio could not be measured directly. Instead, as a proxy the H_2O_2 enhancement ratios are calculated by finding the coordinates of the plume of strong H_2O_2-HCN correlation in the AO (generally between −50° or −10°–20° latitudes and between 0.5 and 6.5 km altitude, see Figure 6 for exact portions of flight tracks) and comparing H_2O_2 mixing ratios in these plumes to H_2O_2 at the corresponding latitudes and altitudes of the PO (Table 3). The slope of the H_2O_2-CO linear regression within the AO plumes is also reported. The H_2O_2 mixing ratios encountered in the regions influenced by biomass burning were on average 150–760 pptv (factor of 1.3–2.2 times) higher than those in the corresponding latitudes and altitudes of the PO (Table 3). Similarly, the maximum H_2O_2 mixing ratios were between 670 and 4,470 pptv (factor of 1.2–3.6 times) higher. In each case, the strongest enhancement occurred in the boreal summer (August) followed by the austral summer (February).

Table 3
Ratios and Enhancement Factors for H_2O_2 in the Photochemically Active Biomass Burning Regions Identified

		Avg En[a]	Max En[a]	H_2O_2/CO
February	ATom-2	2.0	3.1	0.010
May	ATom-4	1.6	1.8	0.020
August	ATom-1	2.2	3.6	0.021
October	ATom-3	1.3	1.2	0.021

Note. Average and maximum H_2O_2 enhancement indicates H_2O_2 mixing ratios sampled during biomass burning influence areas compared with those sampled at the corresponding latitudes and altitudes in the Pacific Ocean basin. H_2O_2/CO indicates the ratio of these two species within the BB plumes.
[a]En = enhancement.

This enhancement is likely the result of photochemical processing as the air mass was transported from the continent to the oceanic remote troposphere. The H_2O_2/CO ratios were 2×10^{-2} for most of the deployments, with the exception of February in which the ratio was 1×10^{-2} (Table 3; see the Supporting Information for details on the CO measurement). These values are higher than the 1.5×10^{-3} values measured by Yokelson et al. (2009) and the 4×10^{-3} value measured by Snow et al. (2007), but similar to the $(1–5) \times 10^{-2}$ ratios of Lee et al. (1997). These variations are likely due to the

photochemical age of the air mass sampled: Yokelson et al. (2009) sampled near the source of the fire (0.1–1.5 hr of plume aging) while Snow et al. (2007) and Lee et al. (1997) sampled 4–5 days downwind. The H_2O_2/CO ratio will increase with photochemical aging of the plume; for example, the H_2O_2/CO ratio can increase by a factor of 3–4 within the first 1.5 hr of aging (Yokelson et al., 2009). Thus, the H_2O_2 ratios indicate that the biomass burning influenced air masses sampled during ATom are likely on order of several days old (4–6), with ATom-2 perhaps sampling less photochemically aged air than the other deployments due to the much stronger winds encountered during this season. This estimate is shorter than the back trajectory analysis estimate of 15–20 days since most recent fire influence.

MHP is also elevated in the biomass burning influenced regions, but unlike H_2O_2, it does not exhibit as strong enhancement or as clear correlation with biomass burning tracers. During February and May, the highest MHP mixing ratios were correlated with high HCN and CO and occurred in the same latitude and altitude as for H_2O_2 (Figures S7 and S8 in Supporting Information S1). However, there was significantly more scatter in the hydroperoxide to HCN correlations (R^2 of 0.79 for both seasons for H_2O_2 compared with 0.61 and 0.54, respectively, for MHP). The correlation between MHP and HCN was even weaker for the August and October deployments (R^2 of 0.86 and 0.58, respectively, for H_2O_2 compared with 0.14 and 0.34, respectively, for MHP). The lower correlation of MHP with these biomass burning tracers likely stems from the difference between H_2O_2 and MHP sources: H_2O_2 is solely formed from HO_x cycling while MHP forms from the interaction between both HO_x and CH_4 oxidation (Equations 1 and 3). Unlike H_2O_2, MHP does exhibit an enhancement in mixing ratios that correlates with increased HCN and CO in the northern polar latitudes (above 60°) in August. This high latitude biomass burning influenced air mass is likely highly influenced by continental pollution from N. America and contains higher mixing ratios of CH_4 (100 ppbv or 5% higher CH_4 in polar BB plume than equatorial BB plume), which may lead to higher CH_4 photochemical processing in the sunlit boreal summer month and result in the higher mixing ratios of MHP associated with this plume. Wet scavenging of H_2O_2 due to rain out may have also contributed to higher MHP than H_2O_2 in this plume.

4. Conclusions

The measurements collected using the CIT-CIMS during the four deployments of the ATom Mission show that atmospheric hydroperoxides exhibit highly variable mixing ratios that depend upon latitude, longitude, altitude, and season. H_2O_2 mixing ratios peak in the equatorial latitudes, reaching values as high as 3–6 ppbv in the mid-Atlantic Ocean and 1–3.5 in the mid Pacific Ocean basin, depending on season. H_2O_2 mixing ratios in the mid latitudes varies with season, typically following the shift in sunlight, and declines at a yearly average rate of 5.8 ± 2.0 pptv/degree latitude moving poleward. H_2O_2 peaks between 2 and 4 km above sea level, reflecting the balance between production that peaks at lower altitudes and faster loss due to wet and dry deposition at the surface. In addition, H_2O_2 mixing ratios are highly influenced by regional biomass burning events. Biomass burning plumes originating from Africa permeate the Atlantic Ocean basin and enhance H_2O_2 by a factor of 1.2–3.6 compared to the same latitudes in the Pacific Ocean basin.

MHP mixing ratios are similar to those of H_2O_2, but vary less with latitude. MHP mixing ratios are typically highest in the equatorial region, reaching maximum values within the atmospheric column of 3.0–8.6 ppbv in the Pacific Ocean and 2.5–6.7 ppbv in the Atlantic Ocean basin. These values are higher than those typically reported in the remote atmosphere (Lee et al., 2000; O'Sullivan et al., 1999; Slemr & Tremmel, 1994; Snow et al., 2007). Higher MHP mixing ratios span from −60° to 60°, with some variation that follows the seasonal variations in sunlight. MHP mixing ratios decline at a yearly average rate of 8.1 ± 2.5 pptv/degree latitude moving poleward. Like H_2O_2, MHP mixing ratios are highest in the lower troposphere just above the marine boundary layer, and exhibit a smaller gradient between the top of the marine boundary layer and the ocean surface than H_2O_2. MHP is not as strongly influenced as H_2O_2 by regional biomass burning emissions in the Atlantic Ocean basin, but this organic hydroperoxide does show some correlation with biomass burning tracers in February and May. In addition, MHP shows some correlation with biomass burning influenced air in the northern polar latitudes in August which does not similarly exist for H_2O_2, likely due to either the differences in the sources or the differences in wet scavenging between these two hydroperoxides.

The distributions of H_2O_2 and MHP across geographical, altitudinal, and seasonal gradients reveal information about the atmospheric oxidizing capacity. Because these hydroperoxides arise primarily from HO_x chemistry and

in direct competition with NO_x chemistry, regions where H_2O_2 and MHP are present in high mixing ratios are indicative of areas with strong photochemical $HO_2 + RO_2$ chemistry. This data set reveals the extensive nature of $HO_2 + RO_2$ chemistry in the remote troposphere, particularly in the equatorial Atlantic Ocean basin where influences such as emissions from biomass burning can increase HO_x generation. Finally, hydroperoxides alter the atmospheric oxidizing potential themselves through the physical and chemical processes that affect their atmospheric lifetimes. How these processes alter the global distribution of hydroperoxides and their effect on HO_x, including the role of H_2O_2 deposition and convective activity in vertical hydroperoxide transport, as well as comparisons to atmospheric models is explored in a companion paper.

Data Availability Statement

The data presented in this paper are available at https://doi.org/10.3334/ORNLDAAC/1581.

Acknowledgments
Funding for this work was provided by NASA Grant No. NNX15AG61A. Additional support for H. M. A. was provided by the National Science Foundation Graduate Research Fellowship under Grant No. DGE-1144469 and additional support for M. J. K. was provided by the National Science Foundation Grant No. 1524860. The authors would like to thank the organizers of the ATom Mission, particularly S. C. Wofsy and T. B. Ryerson, for providing the opportunity to gather these data. We would also like to thank E. Czech, D. Jordan, and the people at ESPO, as well as the pilots and crew of the DC-8 for the infrastructural support that made these measurements possible.

References

Allen, N. D. C., Abad, G. G., Bernath, P. F., & Boone, C. D. (2013). Satellite observations of the global distribution of hydrogen peroxide (H_2O_2) from ACE. *Journal of Quantitative Spectroscopy and Radiative Transfer*, *115*, 66–77. https://doi.org/10.1016/j.jqsrt.2012.09.008

Andreae, M. O. (2019). Emission of trace gases and aerosols from biomass burning—An updated assessment. *Atmospheric Chemistry and Physics*, *19*, 8523–8546. https://doi.org/10.5194/acp-19-8523-2019

Barth, M. C., Bela, M. M., Fried, A., Wennberg, P. O., Crounse, J. D., St. Clair, J. M., et al. (2016). Convective transport and scavenging of peroxides by thunderstorms observed over the central U.S. during DC3. *Journal of Geophysical Research: Atmospheres*, *121*, 4272–4295. https://doi.org/10.1002/2015jd024570

Brune, W. H., Miller, D. O., Thames, A. B., Allen, H. M., Apel, E. C., Blake, D. R., et al. (2020). Exploring oxidation in the remote free troposphere: Insights from atmospheric tomography (ATom). *Journal of Geophysical Research: Atmospheres*, *125*, e2019JD031685. https://doi.org/10.1029/2019jd031685

Chang, W., Lee, M., & Heikes, B. G. (2004). One-dimensional photochemical study of H_2O_2, CH_3OOH, and HCHO in the marine boundary layer during Pacific Exploratory Mission in the Tropics (PEM-Tropics) B. *Journal of Geophysical Research*, *109*, D06307. https://doi.org/10.1029/2003jd004256

Crounse, J. D., McKinney, K. A., Kwan, A. J., & Wennberg, P. O. (2006). Measurement of gas-phase hydroperoxides by chemical ionization mass spectrometry. *Analytical Chemistry*, *78*, 6726–6732. https://doi.org/10.1021/ac0604235

Fischer, H., Pozzer, A., Schmitt, T., Jöckel, P., Klippel, T., Taraborrelli, D., & Lelieveld, J. (2015). Hydrogen peroxide in the marine boundary layer over the South Atlantic during the OOMPH cruise in March 2007. *Atmospheric Chemistry and Physics*, *15*, 6971–6980. https://doi.org/10.5194/acp-15-6971-2015

Frey, M. M., Stewart, R. W., McConnell, J. R., & Bales, R. C. (2005). Atmospheric hydroperoxides in West Antarctica: Links to stratospheric ozone and atmospheric oxidation capacity. *Journal of Geophysical Research*, *110*, D23301. https://doi.org/10.1029/2005jd006110

Jacob, P., & Klockow, D. (1992). Hydrogen peroxide measurements in the marine atmosphere. *Journal of Atmospheric Chemistry*, *15*, 353–360. https://doi.org/10.1007/bf00115404

Jaeglé, L., Jacob, D. J., Brune, W. H., Faloona, I., Tan, D., Heikes, B. G., et al. (2000). Photochemistry of HO_x in the upper troposphere at northern midlatitudes. *Journal of Geophysical Research*, *105*, 3877–3892. https://doi.org/10.1029/1999jd901016

Jaeglé, L., Jacob, D. J., Wennberg, P. O., Spivakovsky, C. M., Hanisco, T. F., Lanzendorf, E. J., et al. (1997). Observed OH and HO_2 in the upper troposphere suggest a major source from convective injection of peroxides. *Geophysical Research Letters*, *24*, 3181–3184. https://doi.org/10.1029/97gl03004

Kim, Y.-M., Lee, M., Chang, W., Lee, G., Kim, K.-R., & Kato, S. (2007). Atmospheric peroxides over the North Pacific during IOC 2002 shipboard experiment. *Chemosphere*, *69*, 1638–1646. https://doi.org/10.1016/j.chemosphere.2007.05.057

Lee, M., Heikes, B. G., & Jacob, D. J. (1998). Enhancements of hydroperoxides and formaldehyde in biomass burning impacted air and their effect on atmospheric oxidant cycles. *Journal of Geophysical Research*, *103*, 13201–13212. https://doi.org/10.1029/98jd00578

Lee, M., Heikes, B. G., Jacob, D. J., Sachse, G., & Anderson, B. (1997). Hydrogen peroxide, organic hydroperoxide, and formaldehyde as primary pollutants from biomass burning. *Journal of Geophysical Research*, *102*, 1301–1309. https://doi.org/10.1029/96jd01709

Lee, M., Heikes, B. G., & O'Sullivan, D. W. (2000). Hydrogen peroxide and organic hydroperoxide in the troposphere: A review. *Atmospheric Environment*, *34*, 3475–3494. https://doi.org/10.1016/s1352-2310(99)00432-x

Li, Q., Jacob, D. J., Bey, I., Yantosca, R. M., Zhao, Y., Kondo, Y., & Notholt, J. (2000). Atmospheric hydrogen cyanide (HCN): Biomass burning source, ocean sink? *Geophysical Research Letters*, *27*, 357–360. https://doi.org/10.1029/1999gl010935

Mao, J., Jacob, D. J., Evans, J. R., Olson, J. R., Ren, X., Brune, W. H., et al. (2010). Chemistry of hydrogen oxide radicals (HO_x) in the Arctic troposphere in spring. *Atmospheric Chemistry and Physics*, *10*, 5823–5838. https://doi.org/10.5194/acp-10-5823-2010

Martin, D., Tsivou, M., Bonsang, B., Abonnel, C., Carsey, T., Springer-Young, M., et al. (1997). Hydrogen peroxide in the marine atmospheric boundary layer during the Atlantic Stratocumulus Transition Experiment/Marine Aerosol and Gas Exchange experiment in the eastern subtropical North Atlantic. *Journal of Geophysical Research*, *102*, 6003–6015. https://doi.org/10.1029/96jd03056

Nguyen, T. B., Crounse, J. D., Teng, A. P., Clair, S. J. M., Paulot, F., Wolfe, G. M., & Wennberg, P. O. (2015). Rapid deposition of oxidized biogenic compounds to a temperate forest. *Proceedings of the National Academy of Sciences*, *112*, E392–E401. https://doi.org/10.1073/pnas.1418702112

Olson, J. R., Crawford, J. H., Brune, W., Mao, J., Ren, X., Fried, A., et al. (2012). An analysis of fast photochemistry over high northern latitudes during spring and summer using in-situ observations from ARCTAS and TOPSE. *Atmospheric Chemistry and Physics*, *12*, 6799–6825. https://doi.org/10.5194/acp-12-6799-2012

O'Sullivan, D. W., Heikes, B. G., Lee, M., Chang, W., Gregory, G. L., Blake, D. R., & Sachse, G. W. (1999). Distribution of hydrogen peroxide and methyl hydroperoxide over the Pacific and South Atlantic Oceans. *Journal of Geophysical Research*, *104*, 5635–5646.

Paulot, F., Crounse, J. D., Kjaergaard, H. G., Kroll, J. H., Seinfeld, J. H., & Wennberg, P. O. (2009). Isoprene photooxidation: New insights into the production of acids and organic nitrates. *Atmospheric Chemistry and Physics*, *9*, 1479–1501. https://doi.org/10.5194/acp-9-1479-2009

Prather, M. J., Flynn, C. M., Zhu, X., Steenrod, S. D., Strode, S. A., Fiore, A. M., et al. (2018). How well can global chemistry models calculate the reactivity of short-lived greenhouse gases in the remote troposphere, knowing the chemical composition. *Atmospheric Measurement Techniques*, *11*, 2653–2668. https://doi.org/10.5194/amt-11-2653-2018

Prather, M. J., Zhu, X., Flynn, C. M., Strode, S. A., Rodriquez, J. M., Steenrod, S. D., et al. (2017). Global atmospheric chemistry—Which air matters. *Atmospheric Chemistry and Physics*, *17*, 9081–9102. https://doi.org/10.5194/acp-17-9081-2017

Randerson, J. T., Chen, Y., van derWerf, G. R., Rogers, B. M., & Morton, D. C. (2012). Global burned area and biomass burning emissions from small fires. *Journal of Geophysical Research*, *117*, G04012. https://doi.org/10.1029/2012jg002128

Reeves, C. E., & Penkett, S. A. (2003). Measurements of peroxides and what they tell us. *Chemical Reviews*, *103*, 5199–5218. https://doi.org/10.1021/cr0205053

Rinsland, C. P., Coheur, P. F., Herbin, H., Clerbaux, C., Boone, C., Bernath, P., & Chiou, L. S. (2007). Detection of elevated tropospheric hydrogen peroxide (H_2O_2) mixing ratios in atmospheric chemistry experiment (ACE) subtropical infrared solar occultation spectra. *Journal of Quantitative Spectroscopy & Radiative Transfer*, *107*, 340–348. https://doi.org/10.1016/j.jqsrt.2007.02.009

Roberts, G., Wooster, M. J., & Lagoudakis, E. (2009). Annual and diurnal African biomass burning temporal dynamics. *Biogeosciences*, *6*, 849–866. https://doi.org/10.5194/bg-6-849-2009

Schill, G. P., Froyd, K. D., Bian, H., Kupc, A., Williamson, C., Brock, C. A., et al. (2020). Widespread biomass burning smoke throughout the remote troposphere. *Nature Geoscience*, *13*, 422–427. https://doi.org/10.1038/s41561-020-0586-1

Singh, H. B., Salas, L., Herlth, D., Koyler, R., Czech, E., Viezee, W., et al. (2003). In situ measurements of HCN and CH_3CN over the Pacific Ocean: Sources, sinks, and budgets. *Journal of Geophysical Research*, *108*, 8795. https://doi.org/10.1029/2002jd003006

Slemr, F., & Tremmel, H. G. (1994). Hydroperoxides in the marine troposphere over the Atlantic Ocean. *Journal of Atmospheric Chemistry*, *19*, 371–404. https://doi.org/10.1007/bf00694493

Snow, J. A., Heikes, B. G., Merrill, J. T., Wimmers, A. J., Moody, J. L., & Cantrell, C. A. (2003). Winter-spring evolution and variability of HO_x reservoir species, hydrogen peroxide, and methyl hydroperoxide, in the northern middle to high latitudes. *Journal of Geophysical Research*, *108*, 8362. https://doi.org/10.1029/2002jd002172

Snow, J. A., Heikes, B. G., Shen, H., O'Sullivan, D. W., Fried, A., & Walega, J. (2007). Hydrogen peroxide, methyl hydroperoxide, and formaldehyde over North America and the North Atlantic. *Journal of Geophysical Research*, *112*, D12S07. https://doi.org/10.1029/2006jd007746

St. Clair, J. M., McCabe, D. C., Crounse, J. D., Steiner, U., & Wennberg, P. O. (2010). Chemical ionization tandem mass spectrometer for the in situ measurement of methyl hydrogen peroxide. *Review of Scientific Instruments*, *81*, 094102. https://doi.org/10.1063/1.3480552

Travis, K. R., Heald, C. L., Allen, H. M., Apel, E. C., Arnold, S. R., Blake, D. R., et al. (2020). Constraining remote oxidation capacity with ATom observations. *Atmospheric Chemistry and Physics*, *20*, 7753–7781. https://doi.org/10.5194/acp-20-7753-2020

Van Valin, C. C., Ray, J. D., Boatman, J. F., & Gunter, R. L. (1987). Hydrogen peroxide in air during winter over the south-central United States. *Geophysical Research Letters*, *14*, 1146–1149. https://doi.org/10.1029/gl014i011p01146

Walcek, C. J. (1987). A theoretical estimate of O_3 and H_2O_2 dry deposition over the northeast United States. *Atmospheric Environment*, *21*, 2649–2659. https://doi.org/10.1016/0004-6981(87)90196-x

Weller, R., & Schrens, O. (1993). H_2O_2 in the marine troposphere and seawater of the Atlantic Ocean (48°–63°). *Geophysical Research Letters*, *20*, 125–128. https://doi.org/10.1029/93gl00065

Yokelson, R. J., Crounse, J. D., DeCarlo, P. F., Karl, T., Urbanski, S., Atlas, E., et al. (2009). Emissions from biomass burning in the Yucatan. *Atmospheric Chemistry and Physics*, *9*, 5785–5812. https://doi.org/10.5194/acp-9-5785-2009